Supplementary information for: Disentangling sequential and concerted fragmentations of molecular polycations with covariant native frame analysis

Joseph W. McManus,[a,‡] Tiffany Walmsley,[a,‡] Kiyonobu Nagaya,[b] James Harries,[c] Yoshiaki Kumagai,[d] Hiroshi Iwayama,[e] Michael N.R. Ashfold,[f] Mathew Britton,[g] Philip H. Bucksbaum,[g] Briony Downes-Ward,[h] Taran Driver,[g] David Heathcote,[a] Paul Hockett,[i] Andrew J. Howard,[g] Edwin Kukk,[j] Jason W. L. Lee,[k] Yusong Liu,[g] Dennis Milesevic,[a] Russell S. Minns,[h] Akinobu Niozu,[l] Johannes Niskanen,[j], Andrew J. Orr-Ewing[f], Shigeki Owada,[m,q] Daniel Rolles,[n] Patrick A. Robertson,[a] Artem Rudenko,[n] Kiyoshi Ueda,[o] James Unwin,[a] Claire Vallance,[a] Michael Burt,[a] Mark Brouard,[a] Ruaridh Forbes,[p,¶] and Felix Allum[a,g,p,*]

[a] *Chemistry Research Laboratory, Department of Chemistry, University of Oxford, Oxford OX1 3TA, United Kingdom*
[b] *Department of Physics, Kyoto University, Kyoto, 606-8502, Japan*
[c] *QST, SPring-8, Kouto 1-1-1, Sayo, Hyogo, 679-5148, Japan*
[d] *TOKYO TECH, Japan*
[e] *UVSOR Synchrotron Facility, Institute for Molecular Science, Okazaki 444-8585, Japan*
[f] *School of Chemistry, University of Bristol, Cantock's Close, Bristol BS8 1TS, U.K.*
[g] *Stanford PULSE Institute, SLAC National Accelerator Laboratory, 2575 Sand Hill Road, Menlo Park, CA 94025*
[h] *Chemistry, University of Southampton, Highfield, Southampton SO17 1BJ, UK*
[i] *National Research Council of Canada, 100 Sussex Dr. Ottawa, ON K1A 0R6, Canada*
[j] *Department of Physics and Astronomy, University of Turku, Turku, FI-20014, Finland*
[k] *Deutsches Elektronen-Synchrotron (DESY), Notkestraße 85, 22607 Hamburg, Germany*
[l] *Graduate School of Advanced Science and Engineering, Hiroshima University, Higashi-Hiroshima 739-8526, Japan*
[m] *RIKEN SPring-8 Center, Sayo, Hyogo, 679-5148, Japan*
[n] *J. R. Macdonald Laboratory, Department of Physics, Kansas State University, Manhattan, KS, 66506, USA*
[o] *Institute of Multidisciplinary Research for Advanced Materials, Tohoku University, Sendai, 980-8577, Japan*
[p] *Linac Coherent Light Source, SLAC National Accelerator Laboratory, Menlo Park, California 94025, USA*
[q] *Japan Synchrotron Radiation Research Institute, Hyogo, Japan*
‡ These authors contributed equally to this work
¶ ruforbes@slac.stanford.edu
* fallum@stanford.edu

1 Covariance calculation

The three-dimensional (3D) covariance calculation method was described in detail in the Supporting Information of Reference 1. Briefly, events in a time-of-flight range characteristic of the ion of interest are selected, for two ions X^+ and Y^+. These events are then transformed from detector position (x and y) and time-of-flight (TOF) to 3D momentum vectors. From pairs of events corresponding to X^+ and Y^+ detected in the same FEL shot, the 'double coincidence' term of the covariance expression ($\langle AB \rangle$) is calculated. The 'single coincidence' term ($\langle A \rangle \langle B \rangle$) is calculated similarly, but from all pairs of X^+ and Y^+ ions across a random sample of laser shots. The two primary changes to the analysis method in the current work are i) the transformation to the native frame, which can be done on each individual pair of ions in the calculation and ii) the use of contingent covariance.

An example of the double and single coincidence terms, and resulting covariance, are shown in Fig. S1. The double coincidence map (a) contains a large amount of signal from false coincidence, demonstrating that a coincidence analysis is not appropriate for this high count-rate dataset. The false coincidence signal is removed by subtraction of the single coincidence map (b) to produce the covariance map (c).

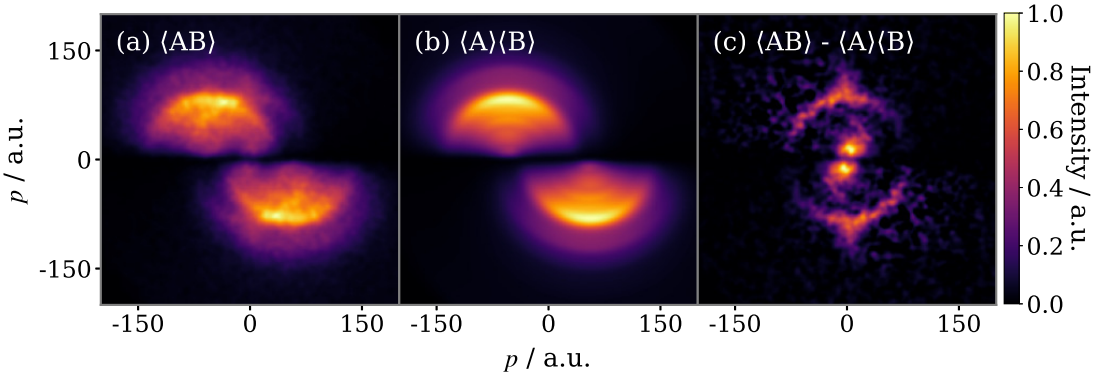

Figure S1: Calculated (a) double and (b) single coincidence terms and (c) covariance for the (I^+ + CH_3^+) ion pair in 2-IP, presented in the native frame.

2 Contingent covariance calculation

An example of the output of the contingent covariance calculation as a function of the number of bins in FEL pulse energy used to divide up the data is shown in Fig. S2. Herein n = 1 corresponds to the regular, non-contingent covariance calculation. Increasing the number of bins reduces the false covariance in the results and improves the signal-to-noise. The contingent covariance figures presented in the main text were produced using 10 bins.

3 Confirming the assignment of the three-body fragmentation channel

To support our assignment of the signal observed and analyzed in the (I^+, CH_3^+) covariance data presented in the main text, additional covariance analysis was performed. In particular, we wished to confirm that the feature assigned to fragmentation of IP^{3+} leads to I^++CH_3^++$C_2H_4^+$ (as opposed to $C_2H_3^+$ + H, etc.). Fig. S3 compares the results from an example covariance analysis between the I^+ and $C_2H_4^+$ fragments to that between the I^+ and CH_3^+ (which is the focus of the discussion in the main paper). Here, an I^+ momentum range was chosen to isolate sequential dissociation features. It can be seen that very similar results are obtained for both isomers when using either pair of covariant ions, as would be expected given our assignment of the three-body fragmentation channel and the use of momentum conservation in the covariance analysis. The poorer signal-to-noise ratio in the I^+ and $C_2H_4^+$ covariance is due to a poorer detection efficiency for the $C_2H_4^+$ ion relative to the CH_3^+ ion under our experimental conditions, and it is for this reason that the (I^+,CH_3^+) covariance is analysed in the

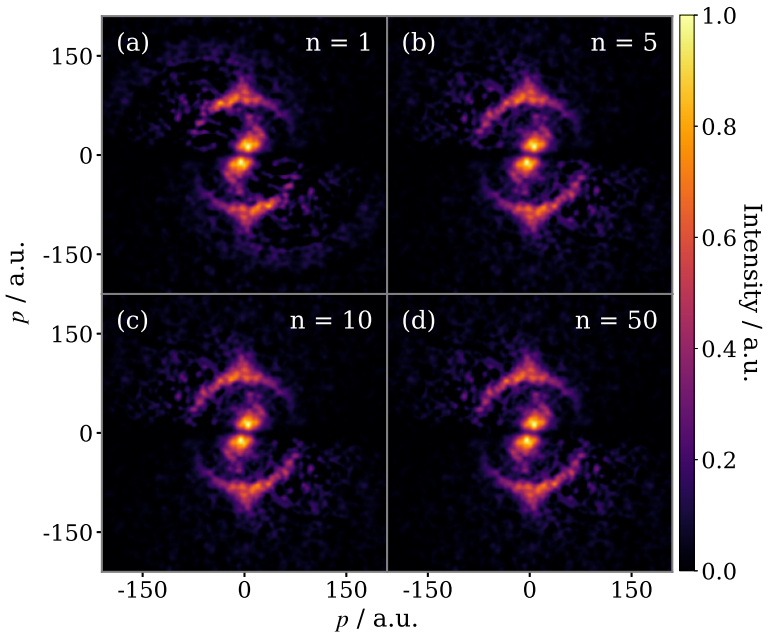

Figure S2: Newton diagrams for the breakup of 2-IP$^{2+/3+}$ into (I^+ + CH_3^+ + $C_2H_4/C_2H_4^+$) as a function of the quantity of bins (n) used in the contingent covariance calculation. n = 1 corresponds to a regular, non-contingent covariance calculation.

main manuscript. Finally we note that no signal resembling that of a sequential dissociation is seen for other $C_2H_x^+$ ions in covariance with the I^+ ion.

4 Classical simulation of the three-body sequential breakup of polycations

4.1 Description of the method used

We model the Coulomb explosion process using simple, classical trajectory calculations of point charges interacting exclusively under Coulomb's law. To recreate the sequential three-body breakup of the IP trication the simulation is executed in two distinct steps, which model the primary and secondary fragmentation steps respectively. For the first step, the loss of I^+, we consider the Coulomb explosion of I^+ and $C_3H_7^{2+}$. The simulation is initiated from the molecule's neutral ground state geometry, in its lowest energy, fully staggered conformation, and the charge on each fragment is located at its centre-of-mass (COM). For each individual simulation, the lifetime of $C_3H_7^{2+}$ is determined by randomly sampling on the curve described by eqn. 4 in the main manuscript. The trajectories of the two fragments are propagated until this lifetime has been met, at which the point the further breakup of $C_3H_7^{2+}$ is considered to occur, beginning the second step of the simulation.

At this point, $C_3H_7^{2+}$ is replaced in the simulation by CH_3^+ and $C_2H_4^+$, in the same geometry as in the initial molecular structure. The two fragments are once more treated as point charges placed on the adjacent carbon atoms of the two fragments. Finally, to model the rotation of the propyl dication during its lifetime, the point charges are rotated through the angle given by the product of the intermediate lifetime and rotational period. This rotation is about the *c*-axis for the 1-propyl fragment, and the *a*-axis of the 2-propyl fragment, as illustrated in Fig. 9 and 10 of the main text. The trajectories of the I^+, CH_3^+ and $C_2H_4^+$ ions are then propagated until they have all reached their tangential velocities.

Modifications made to account for changes in the nuclear geometry of the propyl dication were performed by altering the spatial arrangement of the CH_3^+ and $C_2H_4^+$ point charges prior to the second step of the simulation. To reproduce the experimental kinetic energy release (KER) of the (CH_3^+, $C_2H_4^+$) Coulomb explosion, the separation of the CH_3^+ and $C_2H_4^+$ point charges is determined, for each individual simulation, by sampling on a Gaussian distribution with centre 5.3 eV and width 0.9 eV, then converting to distance using Coulomb's law. Similarly, to crudely approximate the vibrational motion of

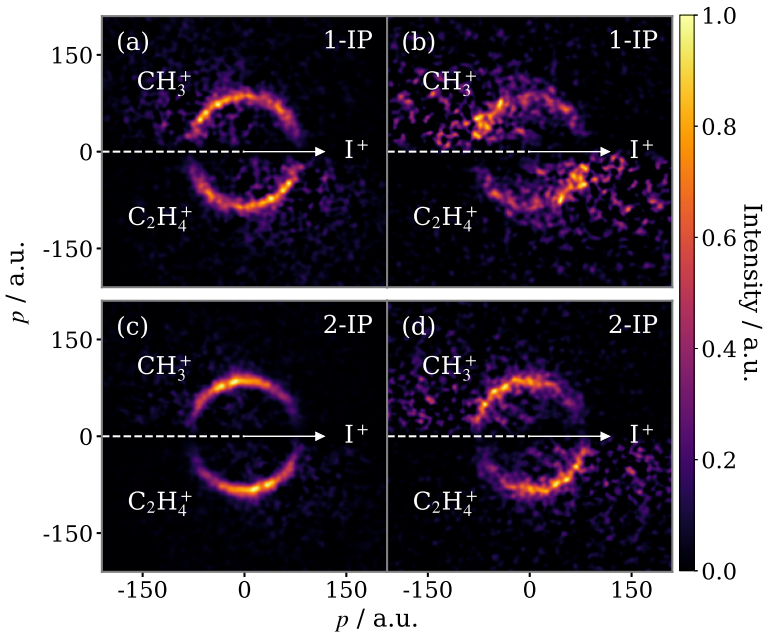

Figure S3: Newton diagrams for the sequential breakup of (a) + (b) 1-IP^{3+} and (c) + (d) 2-IP^{3+} into (I^+ + CH_3^+ + $C_2H_4^+$) in the COM frame of the secondary dissociation $C_3H_7^{2+} \rightarrow CH_3^+ + C_2H_4^+$. Panels (a) and (c) have been produced using a two-fold contingent covariance analysis between I^+ and CH_3^+, whilst panels (b) and (d) were produced using (I^+, $C_2H_4^+$) covariance. The momentum of third fragment is deduced from momentum conservation in this frame. The matching momentum distribution between (a) and (b), (c) and (d), confirms our assignment of the third fragment.

the propyl dication, the C-C-C bond angle in each simulation is selected from a Gaussian distribution, centered on the original bond angle, with a width of 30°. To simulate distortion of the propyl dication bond angle we shift the centre of this distribution by ±20°. The out-of-plane rotation is applied in the same way and is considered to be about the b-axis for both the 1- and 2-propyl fragments.

4.2 The effect of model parameters

The two key parameters which control the output of the simulation for a given molecular structure are the rotational period (T_R) and characteristic lifetime (τ) of the propyl dication intermediate. Fig. S4 demonstrates the effect of increasing τ whilst keeping T_R fixed for both 1-IP and 2-IP. These simulations were performed using the version of the model which incorporates the effective separation of the CH_3^+ and $C_2H_4^+$ ions, and uses a Gaussian distribution of the C-C-C bond angle to crudely approximate the vibrational motion of the $C_3H_7^{2+}$ intermediate. As the lifetime is increased, the simulated fragmentation transitions from essentially concerted to sequential, with corresponding changes in both the KERs and relative angles in the native frame. In the case of 1-IP, for sufficiently long lifetimes of the dication intermediate, an essentially isotropic recoil angle is produced, as expected. In the 2-IP case, for a long lifetime intermediate the signal is still constrained to a relatively narrow angular range. As discussed in detail in the main manuscript, this is due to to the different assumed axis of rotation of the propyl intermediate, restricting the orientations sampled with respect to the I^+ momentum vector.

Shown in Fig. S5 is the influence of changing T_R and whilst keeping the ratio $\frac{T_R}{\tau}$ constant (in this case, the ratio equals one half). The parameters used to produce the figures presented in the main text are the same as for the simulations shown in the central panels of Fig. S4 and S5.

4.3 Simulated concerted three-body breakup of the 1-iodopropane tri-cation

The isolated signal for the three-body concerted fragmentation of 1-IP^{3+} is compared in Fig. S6 with the results of the simulation for the same process, with $\tau = 25$ fs. Similar to the covariance map for concerted

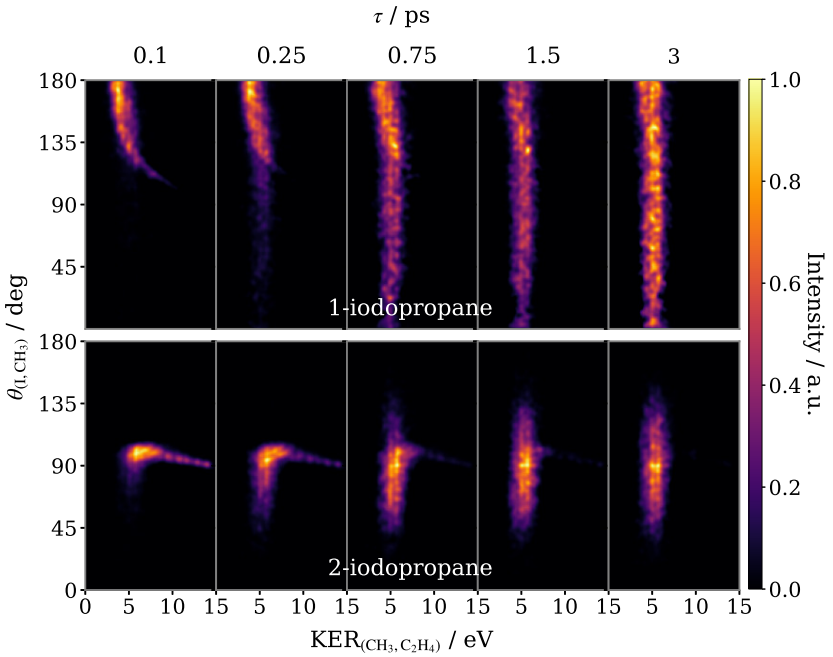

Figure S4: Simulated covariance maps for concerted three-body breakup of 1-IP^{3+} (upper) and 2-IP^{3+} (lower) as a function of KER of the secondary products ($\mathrm{KER}_{(\mathrm{CH_3},\mathrm{C_2H_4})}$) and the relative recoil angle between the iodine and methyl ions ($\theta_{(\mathrm{I},\mathrm{CH_3})}$), showing how the output of the simulation varies as the lifetime of the propyl dication intermediate, τ. The lifetime for each simulation is indicated along the top row. A constant rotational period of the dication intermediate of 0.75 ps is used.

fragmentation of 2-IP^{3+} (Fig. 8 in the main text), we observe a feature narrowly distributed around 90°, with a broad KER range. In this case, however, the simulation is less successful at reproducing the experimental feature. It roughly captures the observed KER range, but predicts a much more significant angular dependence, with the relative recoil angle rising as the KER of the secondary dissociation process decreases. Panel (a) does appear to show signal at obtuse recoil angles, but it is difficult to conclude whether it is significant due to the low signal-to-noise ratio in the covariance map. Whilst the precise cause of this relatively poor agreement is difficult to ascertain, it is likely to involve more complex nuclear dynamics occurring in the 1-IP trication during its concerted fragmentation that is not captured in the simple model.

5 Additional data analysis

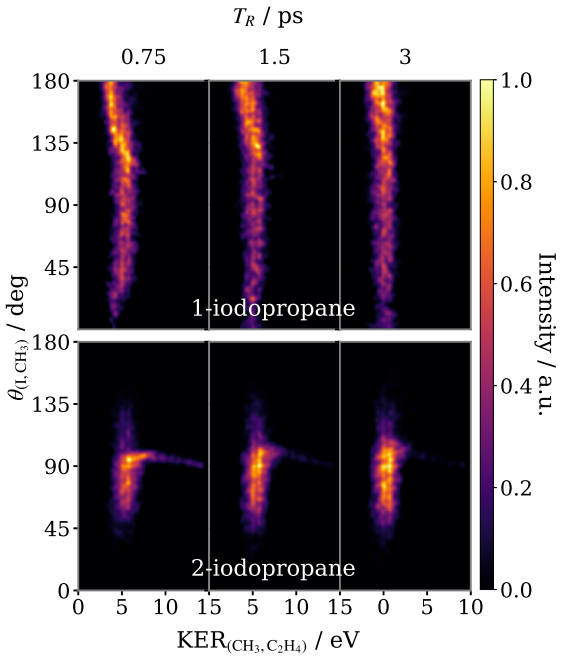

Figure S5: Simulated covariance maps for concerted three-body breakup of 1-IP^{3+} (upper) and 2-IP^{3+} (lower) as a function of KER of the secondary products ($KER_{(CH_3,C_2H_4)}$) and the relative recoil angle between the iodine and methyl ions ($\theta_{(I,CH_3)}$), showing how the output of the simulation varies as the rotational period and characteristic lifetime of propyl dication intermediate are changed in proportion. The rotational period for each simulations is indicated along the top row. All simulations use a lifetime equal to half the rotational period.

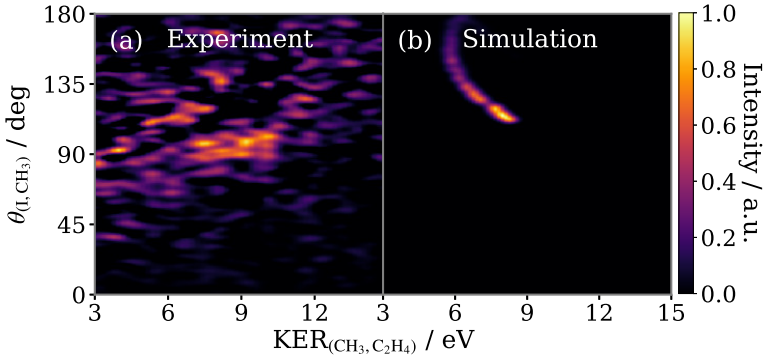

Figure S6: Experimental (a) and simulated (b) covariance maps for concerted three-body breakup of 1-IP^{3+} as a function of the KER of the secondary products ($KER_{(CH_3,C_2H_4)}$) and the relative recoil angle between the iodine and methyl ions ($\theta_{(I,CH_3)}$). Each panel is normalised separately.

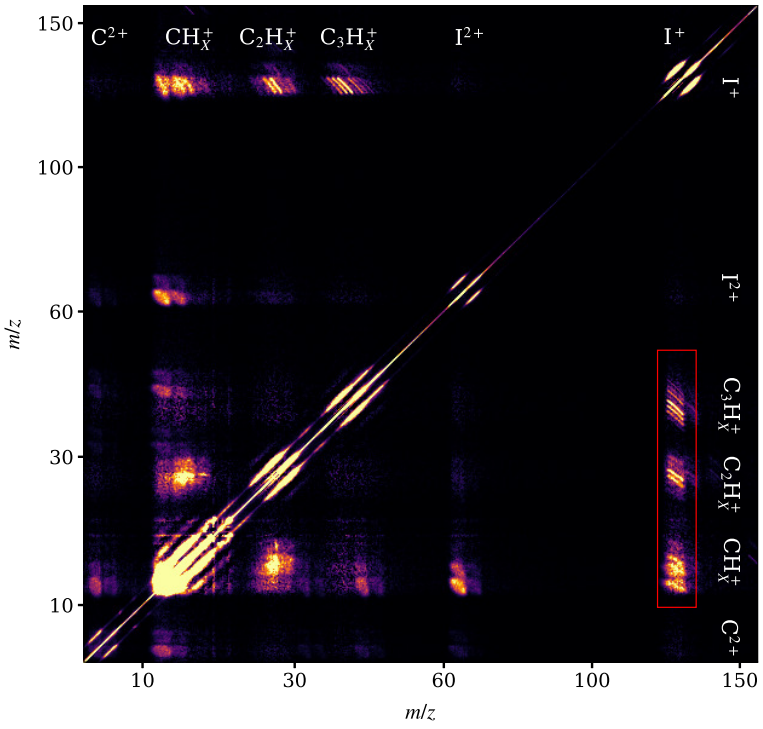

Figure S7: Contingent TOF-TOF covariance map calculated for the XUV ionisation of 1-IP. Correlations between the singly charged iodine and alkyl fragments are highlighted by the red box, which is shown enlarged in Fig. 4 (f) in the main manuscript.

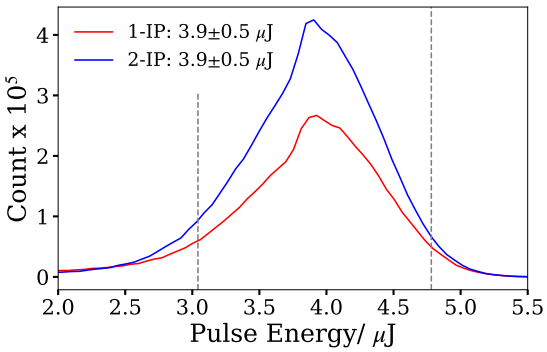

Figure S8: FEL pulse energy distribution at the interaction region for both 1-IP (red) and 2-IP (blue). Gaussian fitting was used to extract the average energy and corresponding standard deviation, which are listed in the legend. The dashed lines indicate the lower and upper limits of the energy range used in the contingent covariance calculations. The 10 energy bins were normally distributed over this range such that each contained an equal number of unique laser shots.

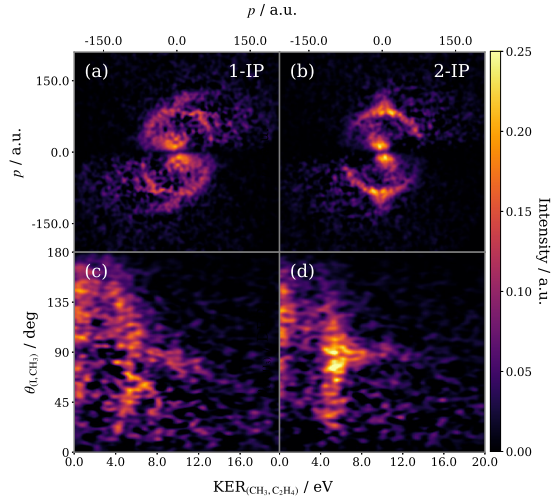

Figure S9: Covariance between the I^+ and CH_3^+ without any filtering of the momentum of the I^+ ion. Panels a) and b) display the covariances for 1-IP and 2-IP respectively as a Newton plot in the native frame, whilst panels c) and d) display these covariances as a function of the KER of the secondary products ($KER_{(CH_3,C_2H_4)}$) and the relative recoil angle between the iodine and methyl ions ($\theta_{(I,CH_3)}$). Each panel is normalised separately.

References

[1] F. Allum, C. Cheng, A. J. Howard, P. H. Bucksbaum, M. Brouard, T. Weinacht and R. Forbes, *The Journal of Physical Chemistry Letters*, 2021, **12**, 8302–8308.